


Borosulfates | *Hot Paper*

Ni[B₂(SO₄)₄] and Co[B₂(SO₄)₄]: Unveiling Systematic Trends in Phyllosilicate Analogue Borosulfates

 Leonard C. Pasqualini,^[a] Oliver Janka,^[b, c] Selina Olthof,^[d] Hubert Huppertz,^[a] Klaus R. Liedl,^[a] Rainer Pöttgen,^[c] Maren Podewitz,^{*[a]} and Jörn Bruns^{*[e]}

Abstract: Borosulfates are compounds analogous to silicates, with heteropolyanionic subunits of vertex-linked (SO₄)- and (BO₄)-tetrahedra. In contrast to the immense structural diversity of silicates, the number of borosulfates is yet very limited and the extent of their properties is still unknown. This is particularly true for representatives with phyllosilicate and tectosilicate analogue anionic substructures. Herein, we present Ni[B₂(SO₄)₄] and Co[B₂(SO₄)₄], two new borosulfates with phyllosilicate analogue topology. While the anionic subunits of both structures are homeotypic, the positions of the

charge compensating cations differ significantly: Ni^{II} is located between the borosulfate layers, while Co^{II}—in contrast—is embedded within the layer. Detailed analysis of these two structures based on single-crystal X-ray diffraction, magnetochemical investigations, X-ray photoelectron spectroscopy, and quantum chemical calculations, unveiled the reasons for this finding. By *in silico* comparison with other divalent borosulfates, we uncovered systematic trends for phyllosilicate analogues leading to the prediction of new species.

Introduction

Synthesis, characterization, and technical applications of silicates is an ever-ongoing field of research. The structural variety of silicates is immense, resulting in a manifold of structure-related properties. In addition to compounds with the monomeric oxoanions consisting of [SiO₄]⁴⁻ units, silicates are able to branch into further directions by vertex-linking of (SiO₄)-tetra-

hedra. Friedrich Liebau established a crystal chemical classification, to which textbooks refer to even today.^[1] Accordingly, silicates are distinguished by their extent of poly-condensation, starting formally from the *ortho*-silicic acid as well as by the branching of the vertex-linked network of (SiO₄)-tetrahedra. Referring to Liebau's classification, minerals with the monomeric anion [SiO₄]⁴⁻ are denoted as nesosilicates. Single condensation leads to sorosilicates with the [Si₂O₇]⁶⁻ anions. Compounds with constantly enlarged anionic chains are classified as inosilicates, whereas a ring closure leads to cyclosilicates with typical anions being [Si₃O₉]⁶⁻, [Si₄O₁₂]⁸⁻ and [Si₆O₁₈]¹²⁻. A very prominent representative of the inosilicates is beryl Al₂Be₃[Si₆O₁₈].^[2] Anionic subunits with a layered arrangement are called phyllosilicates. If all oxygen atoms of the (SiO₄)-tetrahedra bridge between two silicon atoms, a 3D network with the sum formula of quartz (SiO₂) occurs, such compounds are denoted as tectosilicates.

Due to the relevance of silicates for a variety of technical applications, several substitution variants were explored to further broaden the scope of these. If silicon atoms are partially replaced by aluminum atoms, aluminosilicates are formed.^[3] Therefore, charge-balancing cations need to be inserted. Most prominent representatives are zeolites, which are, for example, used as ion exchange materials or for gas adsorption.^[4]

After the development of alumophosphates^[5] and borophosphates^[6] as further substitution variants of silicates, the first borosulfate, K₅[B(SO₄)₄], was reported in 2012.^[7] This compound exhibits the oligomeric oxoanion [B(SO₄)₄]⁵⁻ with boron being in the center of four (SO₄)-tetrahedra. In general, borosulfates are inorganic metal or non-metal salts with an oxoanionic substructure consisting of vertex-sharing boron and sulfur-centred tetrahedra. Ideally, the (BO₄)- and (SO₄)-units are

[a] L. C. Pasqualini, Prof. Dr. H. Huppertz, Prof. Dr. K. R. Liedl, Dr. M. Podewitz
 University of Innsbruck
 Institute of General Inorganic and Theoretical Chemistry
 Innrain 80–82, 6020 Innsbruck (Austria)
 E-mail: maren.podewitz@uibk.ac.at

[b] Dr. O. Janka
 Universität des Saarlandes, Anorganische Festkörperchemie
 Campus C4 1, 66123 Saarbrücken (Germany)

[c] Dr. O. Janka, Prof. Dr. R. Pöttgen
 Westfälische Wilhelms-Universität Münster
 Institut für Anorganische und Analytische Chemie
 Corrensstrasse 30, 48149 Münster (Germany)

[d] Dr. S. Olthof
 Institute of Physical Chemistry, University of Cologne
 Greinstrasse 4–6, 50939 Cologne (Germany)

[e] Dr. J. Bruns
 Institute of Inorganic Chemistry, University of Cologne
 Greinstrasse 6, 50939 Cologne (Germany)
 E-mail: j.bruns@uni-koeln.de

Supporting information and the ORCID identification number(s) for the author(s) of this article can be found under:
<https://doi.org/10.1002/chem.202002221>.

© 2020 The Authors. Published by Wiley-VCH GmbH. This is an open access article under the terms of the Creative Commons Attribution Non-Commercial NoDerivs License, which permits use and distribution in any medium, provided the original work is properly cited, the use is non-commercial and no modifications or adaptations are made.

perfectly alternating within the anionic network.^[8] However, also B–O–B^[8d,9] and S–O–S^[8a,c,h] bridges can occur. Hitherto, borosulfates were synthesized with anionic^[8,9b–d] and even with uncharged^[9a] tetrahedral networks. To the best of our knowledge, to date only 57 borosulfates have been properly characterized by means of X-ray single-crystal analysis.^[8,9] For purely S–O–B bridged species the number decreases to 39.^[8,10,11] To stick to the latter, the majority of these borosulfates exhibit oligomeric oxoanions or infinite anionic chains. Further, branching of the anionic network is rare. Li[B(SO₄)₂] is, thus far, the only borosulfate exhibiting a 3D network of perfectly alternating (SO₄)⁻ and (BO₄)⁻ tetrahedra.^[8a] Phyllosilicate analogue substructures of purely S–O–B bridged species are only known for the compounds Ca[B₂(SO₄)₄],^[8b] Mg[B₂(SO₄)₄],^[9d] Zn[B₂(SO₄)₄],^[11] and Mn[B₂(SO₄)₄].^[11]

In this work, we report two new transition-metal representatives with phyllosilicate analogue anionic substructures. Ni[B₂(SO₄)₄] and Co[B₂(SO₄)₄] feature anionic layers of four- and twelve-membered rings formed by vertex-shared (SO₄)⁻ and (BO₄)⁻ tetrahedra. Both anionic substructures are homeotypic to each other. However, the positions of the divalent cations with respect to the anionic layers differ significantly. All cobalt cations reside within the center of the twelve-membered rings, whereas the nickel cations are exclusively located above and underneath the rings.

In the following, we present the solvothermal synthesis, as well as the rigorous characterization of Ni[B₂(SO₄)₄] and

Co[B₂(SO₄)₄]. Analysis of the crystal structure and the bonding situation were complemented by magnetochemical measurements as well as X-ray photoelectron spectroscopy (XPS) to determine the oxidation state of Co in Co[B₂(SO₄)₄]. Quantum chemical calculations further aided the characterization. By comparison with other previously reported borosulfates, these computational studies allowed us to rationalize the different cation positions with respect to the anionic layers and to predict new phyllosilicate analogous borosulfates of divalent cations.

Results and Discussion

The synthesis of Ni[B₂(SO₄)₄] and Co[B₂(SO₄)₄] was performed using a solvothermal reaction between a suitable metal source, in this case NiO and Co₃O₄, H₃BO₃, and oleum (65% SO₃) in evacuated torch-sealed glass ampoules at elevated temperature (for details see experimental section).

Structural analysis

Ni[B₂(SO₄)₄] crystallizes in the monoclinic space group *C2/c* ($a = 17.311(1)$, $b = 5.2682(4)$, $c = 14.326(1)$ Å, $\beta = 126.119(2)^\circ$; see Table 1 and experimental section for further crystal data and structural refinement details) and is isotypic to Mg[(B₂(SO₄)₄)]^[9d]

The crystal structure reveals a layered anionic substructure of vertex-shared (SO₄)⁻ and (BO₄)⁻ tetrahedra, charge compen-

Table 1. Crystal data and structure refinement for Ni[B₂(SO₄)₄] and Co[B₂(SO₄)₄].

Empirical formula	B ₂ NiO ₁₆ S ₄	B ₂ CoO ₁₆ S ₄
formula weight	464.57	464.79
<i>T</i> [K]	173(2)	183(2)
crystal system	monoclinic	monoclinic
space group	<i>C2/c</i> (no. 15)	<i>P2₁/n</i> (no. 14)
<i>a</i> [Å]	17.311(1)	7.8481(3)
<i>b</i> [Å]	5.2682(4)	8.1134(3)
<i>c</i> [Å]	14.326(1)	9.0453(3)
β [°]	126.119(2)	111.324(1)
volume [Å ³]	1055.3	536.53
<i>Z</i>	4	2
ρ_{calc} [g cm ⁻³]	2.92	2.88
absorption coefficient [mm ⁻¹]	2.7	2.5
<i>F</i> (000)	920	458
crystal size [mm ³]	0.05 × 0.05 × 0.04	0.09 × 0.07 × 0.06
radiation	Mo _{Kα1} ($\lambda = 0.7093$ Å)	Mo _{Kα1} ($\lambda = 0.7093$ Å)
2θ range for data collection	5.8 to 75.8°	5.9 to 77.0°
index ranges	−29 ≤ <i>h</i> ≤ 29 −9 ≤ <i>k</i> ≤ 9 −24 ≤ <i>l</i> ≤ 24	−13 ≤ <i>h</i> ≤ 13 −14 ≤ <i>k</i> ≤ 14 −15 ≤ <i>l</i> ≤ 15
reflections collected	29705	19704
independent reflections	2848 [<i>R</i> _{int} = 0.0505]	3012 [<i>R</i> _{int} = 0.0186]
completeness to θ	100%	99.9%
absorption correction	multi-scan	multi-scan
refinement method	full-matrix least-squares on <i>F</i> ²	full-matrix least-squares on <i>F</i> ²
data/restraints/parameters	2848/ 0/ 106	3012/ 0/ 107
goodness-of-fit on <i>F</i> ²	1.033	1.156
final <i>R</i> indexes [<i>I</i> ≥ 2 σ (<i>I</i>)]	<i>R</i> ₁ = 0.0262 <i>wR</i> ₂ = 0.0555	<i>R</i> ₁ = 0.0170 <i>wR</i> ₂ = 0.0458
final <i>R</i> indexes [all data]	<i>R</i> ₁ = 0.0384 <i>wR</i> ₂ = 0.0591	<i>R</i> ₁ = 0.0181 <i>wR</i> ₂ = 0.0462
largest diff. peak/hole/e ⁻ /Å ⁻³	+ 0.61/−0.92	+ 0.75/−0.39
CSD number	1894893	1907638

sated by Ni^{II}-cations (Figure 1, left). Invariably, each (BO₄)₂-unit is coordinated by four (SO₄)₂-tetrahedra. The latter exhibits two terminal oxygen atoms and two oxygen atoms acting simultaneously as vertices of the (BO₄)₂-tetrahedra. The O-S-O angles within the (SO₄)₂-tetrahedra range from 100.56(5) to 117.67(6)° and 104.73(5) to 117.15(6)° for the S1 and S2 positions, respectively. There is a significant difference in the S–O bond length between linking and terminal S–O bonds. The latter reveals average values of 1.43 Å, while the distance between sulfur and oxygen atoms within an S–O–B bridge is, on average, 1.53 Å. The B–O bond lengths range from 1.451(2) to 1.486(2) Å and the bond angles from 107.2(1) to 112.3(1)°.

According to the classification of borophosphates by Kniep,^[6a,11] which is based on the pioneering work of Liebau,^[1] the basic building unit (BBU) of both compounds is a 3□:3□ *uB* trimer and the resulting fundamental building unit (FBU) is a 6□:□ < 4□ > □ *oB* ring with a B:S ratio of 1:2, respectively (Figure 2).

By branching of the FBU, the extended anionic substructures occur as *oB* single layers of *vierer* (four-membered) and *zwölfer*

(twelve-membered) rings and can be described with the Niggli formula $\infty^2\{[B(SO_4)_{4/2}]^-\}$ (Figure 3). Comparable anionic layers are also found for other heteropolyanionic compounds like borophosphates, however, the topology of the tetrahedral networks differ.^[6f,g]

In Ni[B₂(SO₄)₄] each *zwölfer* ring shares two (BO₄)(SO₄)(BO₄)-units with two *vierer* rings. Both *vierer* rings are in opposite position to each other and in direct coordination to the *zwölfer* rings. Two further *vierer* rings branch off the *zwölfer* rings via a common (BO₄)₂-tetrahedron and are opposite to each other. Furthermore, each *zwölfer* ring is surrounded by four *zwölfer* rings via a common (BO₄)(SO₄)(BO₄)-unit (Figure 4).

Charge compensation is achieved by Ni^{II} cations, which are packed in between the anionic layers (Figure 3, left), residing exclusively between the *zwölfer* rings, as previously also reported for Mg[B₂(SO₄)₄]^[9d] and Ca[B₂(SO₄)₄].^[8b] The Ni^{II} cations are octahedrally coordinated by six oxygen atoms originating from terminal (SO₄)₂-units and the Ni–O bond lengths range from 2.0152(9) to 2.048(1) Å (Figure S3).

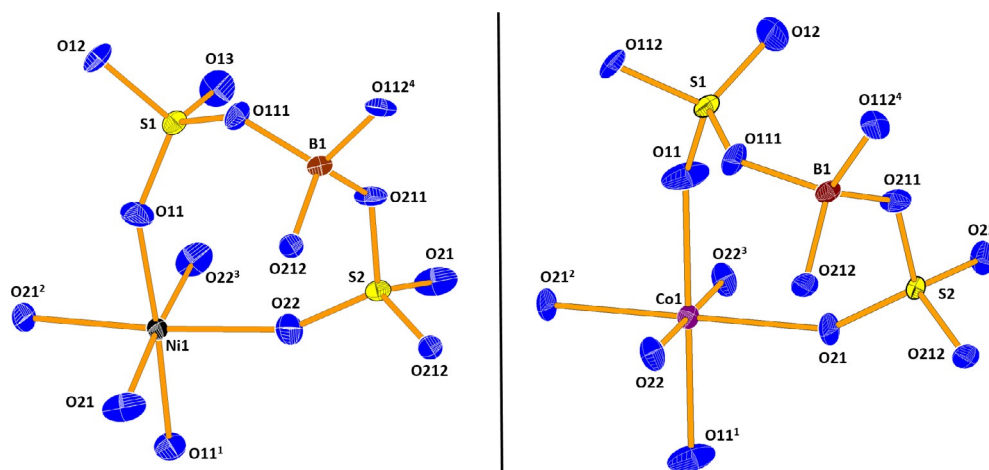


Figure 1. Left: Asymmetric unit of Ni[B₂(SO₄)₄]. The displacement ellipsoids are set on 90% probability level. Selected bond lengths [Å]: S1–O11 1.445(1), S1–O12 1.5271(9), S1–O13 1.412(1), S1–O111 1.5409(9), S2–O21 1.428(1), S2–O22 1.430(1), S2–O211 1.518(1), S2–O212 1.5213(9), B1–O12 1.453(2), B1–O111 1.451(2), B1–O211 1.486(2), B1–O212 1.484(2) (symmetry operators: ¹–x, +y, 1/2–z; ²–x, –1 + y, 1/2–z; ³+x, –1 + y, +z; ⁴1/2–x, 3/2–y, 1–z); Right: Asymmetric unit of Co[B₂(SO₄)₄]. The displacement ellipsoids are set on 90% probability level. Selected bond lengths [Å]: S1–O11 1.4466(6), S1–O12 1.4147(6), S1–O111 1.5270(5), S1–O112 1.5327(5), S2–O21 1.4332(6), S2–O22 1.4297(6), S2–O211 1.5228(5), S2–O212 1.5142(5), B1–O111 1.4610(9), B1–O211 1.4769(9), B1–O212 1.4849(9) (symmetry operators: ¹–x, –y, 1–z; ²–1/2 + x, 1/2–y, –1/2 + z; ³2–x, –1/2 + y, 3/2–z; ⁴3/2–x, 1/2 + y, 1/2–z).

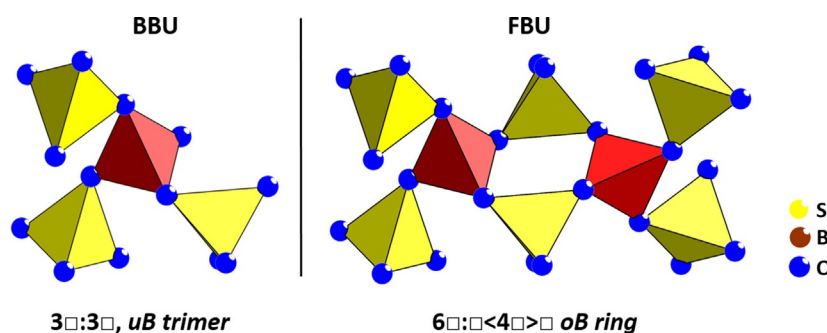


Figure 2. Left: Schematic representation of the basic building unit (BBU) of Ni[B₂(SO₄)₄] and Co[B₂(SO₄)₄]. Right: Fundamental building unit (FBU) of Ni[B₂(SO₄)₄] and Co[B₂(SO₄)₄]. (SO₄)₂ tetrahedra are displayed in yellow, (BO₄)₂ units in red. The nomenclature is based on a concept first presented by Liebau^[1] for silicates, expanded by Kniep^[6a,12] for borophosphates, and now adopted for borosulfates.

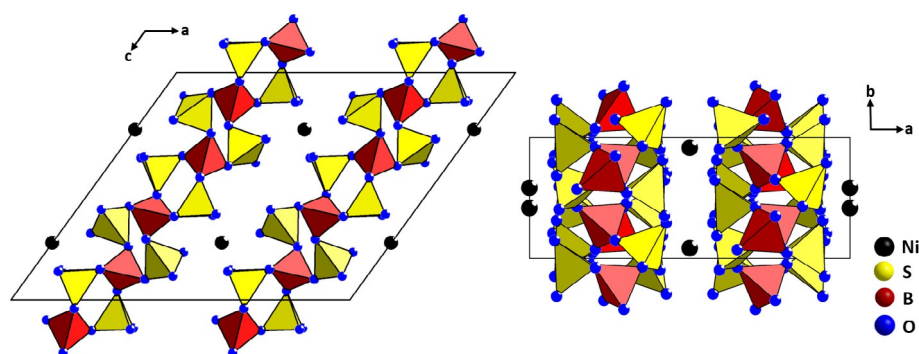


Figure 3. Left: Crystal structure of $\text{Ni}[\text{B}_2(\text{SO}_4)_4]$ in projection on the (010) plane; Right: Crystal structure of $\text{Ni}[\text{B}_2(\text{SO}_4)_4]$ in projection on the (001) plane. $\text{Ni}[\text{B}_2(\text{SO}_4)_4]$ reveals an arrangement of boron-centered infinite anionic layers of vertex-linked (BO_4) - and (SO_4) -tetrahedra. The layers are packed perpendicular to the crystallographic a -axis. The charge compensating Ni^{II} cations reside in between the layers.

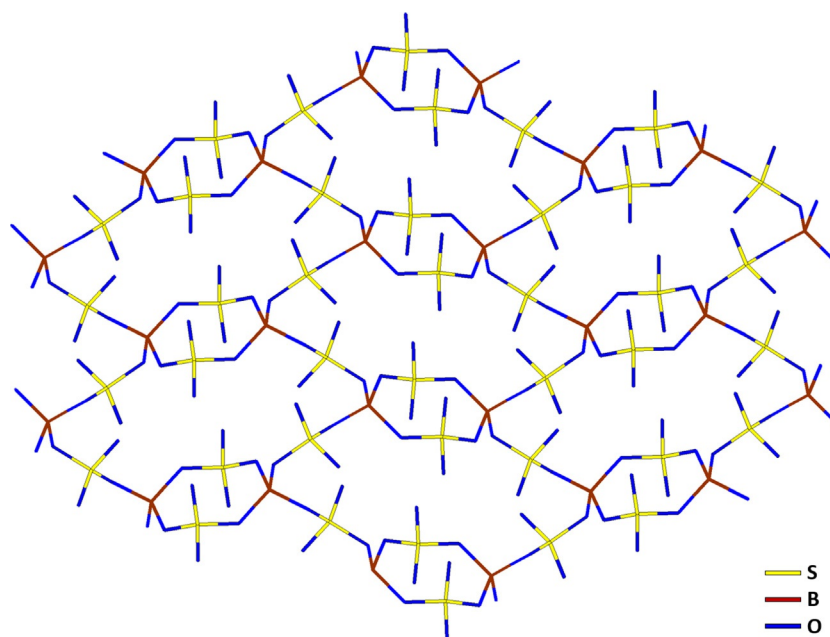


Figure 4. Packing of the anionic layers found for the structure of $\text{Ni}[\text{B}_2(\text{SO}_4)_4]$ depicted as a wire model. The structure exhibits *zwölfer*- and *vierer*-rings of vertex-linked (SO_4) - and (BO_4) -tetrahedra.

The anionic substructure of $\text{Co}[\text{B}_2(\text{SO}_4)_4]$ (monoclinic, $P2_1/n$, $a = 7.8481(3)$, $b = 8.1134(3)$, $c = 9.0453(3)$ Å, $\beta = 111.324(1)^\circ$; see Table 1 and experimental section for further crystal data and structural refinement details) reveals a layered topology and is isotypic to $\text{Zn}[\text{B}_2(\text{SO}_4)_4]$ ^[11] and homeotypic to $\text{Ni}[\text{B}_2(\text{SO}_4)_4]$, $\text{Mn}[\text{B}_2(\text{SO}_4)_4]$,^[11] $\text{Mg}[\text{B}_2(\text{SO}_4)_4]$ ^[9d] as well as $\text{Ca}[\text{B}_2(\text{SO}_4)_4]$ ^[8b] (Figure 1, right). The layers are constituted of vertex-shared (BO_4) - and (SO_4) -tetrahedra, exclusively exhibiting *zwölfer* and *vierer* rings, with all *zwölfer* rings coordinated by two *vierer* rings via common edges and two via common vertices (Figure 5). Furthermore, all *zwölfer* rings are coordinated to four neighbouring *zwölfer* rings.

The boron atoms are fourfold coordinated by (SO_4) -tetrahedra (Figure 1; right), whereas each (SO_4) -tetrahedron bridges two (BO_4) -units, resulting in the Niggli formula $\infty^2\{[\text{B}(\text{SO}_4)_{4/2}]^-\}$ for the anionic substructure. Two oxygen

atoms of the (SO_4) -tetrahedra remain terminal and terminate the anionic layers. The basic building unit (BBU) is a $3\Box:3\Box$ *uB* trimer and the resulting fundamental building unit (FBU) is a $6\Box:\Box < 4\Box > \Box$ *oB* ring with a B:S ratio of 1:2. The S–O bond lengths range from 1.4147(6) (terminal S–O bonds) to 1.5327(5) Å (bridging S–O bonds). The O–S–O bond angles deviate in average 0.2° from the ideal tetrahedral symmetry. The B–O bond lengths fall in the range between 1.4490(9) and 1.4849(9) Å. The O–B–O bond angles vary from $103.18(5)$ to $114.62(6)^\circ$.

Although the composition, connectivity, and branching of all phyllosilicate analogous borosulfate anions is identical, their structures differ clearly, depending on the nature of the charge compensating cations. Generally, three different positions of the cations can be defined, which will in the following be represented by the structures $\text{Co}[\text{B}_2(\text{SO}_4)_4]$, $\text{Ca}[\text{B}_2(\text{SO}_4)_4]$, and

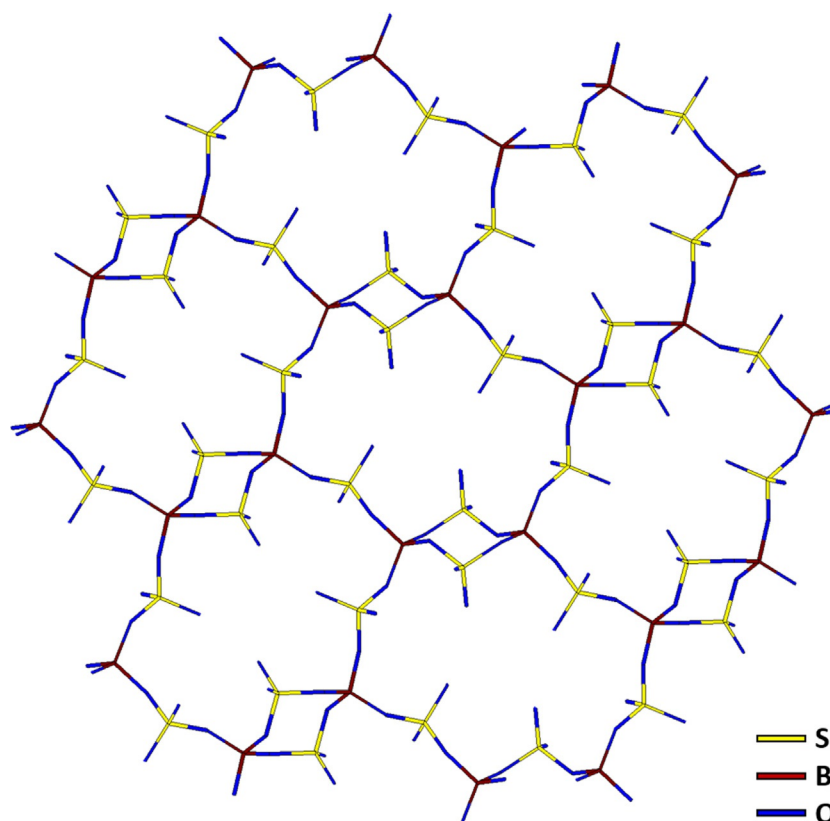


Figure 5. Cut-out of the anionic layers found for the structure of $\text{Co}[\text{B}_2(\text{SO}_4)_4]$ depicted as a wire model. The structure exhibits *zwölfer*- and *vierer*-rings of vertex-linked $(\text{SO}_4)^{-}$ and $(\text{BO}_4)^{-}$ -tetrahedra.

$\text{Ni}[\text{B}_2(\text{SO}_4)_4]$ (Figure 6). In $\text{Ca}[\text{B}_2(\text{SO}_4)_4]$ and $\text{Ni}[\text{B}_2(\text{SO}_4)_4]$, the Ca^{II} and Ni^{II} cations reside above and underneath the center of the *zwölfer* rings. The Ca^{II} cations are coordinated by eight oxygen atoms originating from eight different $(\text{SO}_4)^{-}$ -tetrahedra, four underneath and four above the Ca^{II} cations. The coordination number of the cations is reduced to six for Ni^{II} . Thus, the *zwölfer* rings have to undergo reorientation, resulting in six $(\text{SO}_4)^{-}$ -tetrahedra originating from *zwölfer* rings, three coordinating from underneath and three from above the Ni^{II} cations. $\text{Co}[\text{B}_2(\text{SO}_4)_4]$ reveals the charge compensating cations to be trapped within the *zwölfer* rings of the anionic substructure. The Co^{II} cations are coordinated by four oxygen atoms of the incorporating rings and by one oxygen atom from above and one oxygen from underneath, originating from the neighbouring layers.

Magnetic properties

To further characterize $\text{Ni}[\text{B}_2(\text{SO}_4)_4]$ and $\text{Co}[\text{B}_2(\text{SO}_4)_4]$, for both compounds the temperature dependence of the magnetic susceptibility (χ) was measured at 10 kOe and is plotted along with their inverse susceptibility (χ^{-1}) in Figures 7 and 8(top). The samples show paramagnetism over the whole investigated temperature range, in line with open shell 3d cations; d^8 configuration for Ni^{II} and d^7 for Co^{II} . The extracted magnetic data is summarized in Table 2. The inverse susceptibility was fitted in the temperature range from 75–300 K using the modified

Curie–Weiss law to account for intrinsic diamagnetic contributions and impurities. The susceptibility curves were corrected by the diamagnetic increments of $\chi_0(\text{Co}[\text{B}_2(\text{SO}_4)_4]) = -799 \times 10^{-6} \text{ emu mol}^{-1}$ and $\chi_0(\text{Ni}[\text{B}_2(\text{SO}_4)_4]) = -248 \times 10^{-6} \text{ emu mol}^{-1}$. Both values are significantly larger compared to the calculated sum according to the tabulated Pascal constants of $-172.8 \times 10^{-6} \text{ emu mol}^{-1}$ ($\chi(M^{2+}) = -12 \times 10^{-6} \text{ emu mol}^{-1}$; $\chi(\text{B}^{3+}) = -12 \times 10^{-6} \text{ emu mol}^{-1}$; $\chi(\text{SO}_4^{2-}) = -12 \times 10^{-6} \text{ emu mol}^{-1}$),^[13] suggesting diamagnetic impurities, for example, adhesive H_2SO_4 . The effective magnetic moments were calculated to $\mu_{\text{eff}} = 4.86(1) \mu_{\text{B}}$ ($\text{Co}[\text{B}_2(\text{SO}_4)_4]$) and $\mu_{\text{eff}} = 2.70(1) \mu_{\text{B}}$ ($\text{Ni}[\text{B}_2(\text{SO}_4)_4]$). The obtained moment for the Co compound is higher, compared to the calculated magnetic moment of an expected Co^{2+} cation ($\mu_{\text{calc}}(\text{Co}^{2+}) = 3.87 \mu_{\text{B}}$) and rather in line with a Co^{3+} cation ($\mu_{\text{calc}}(\text{Co}^{3+}) = 4.90 \mu_{\text{B}}$). Spin–orbit coupling, however, can cause deviations from the ideally calculated spin-only moments, as seen in numerous examples, for example, $\text{CoP}_8\text{N}_{14}$

Table 2. Magnetic data for $M[\text{B}_2(\text{SO}_4)_4]$ ($M = \text{Co}, \text{Ni}$) with T_{N} being the Néel temperature, μ_{eff} the effective magnetic moment, μ_{calc} the calculated spin-only moments, θ_{p} the Weiss constant and μ_{sat} the saturation moment at 3 K and 80 kOe.

Compound	T_{N} [K]	$\mu_{\text{eff}}/\mu_{\text{B}}$	$\mu_{\text{calc}}/\mu_{\text{B}}$	θ_{p} [K]	$\mu_{\text{sat}}/\mu_{\text{B}}$
$\text{Co}[\text{B}_2(\text{SO}_4)_4]$	–	4.86(1)	3.87	–27.1(1)	1.76(1)
$\text{Ni}[\text{B}_2(\text{SO}_4)_4]$	3.3(1)	2.70(1)	2.83	–3.3(1)	1.71(1)

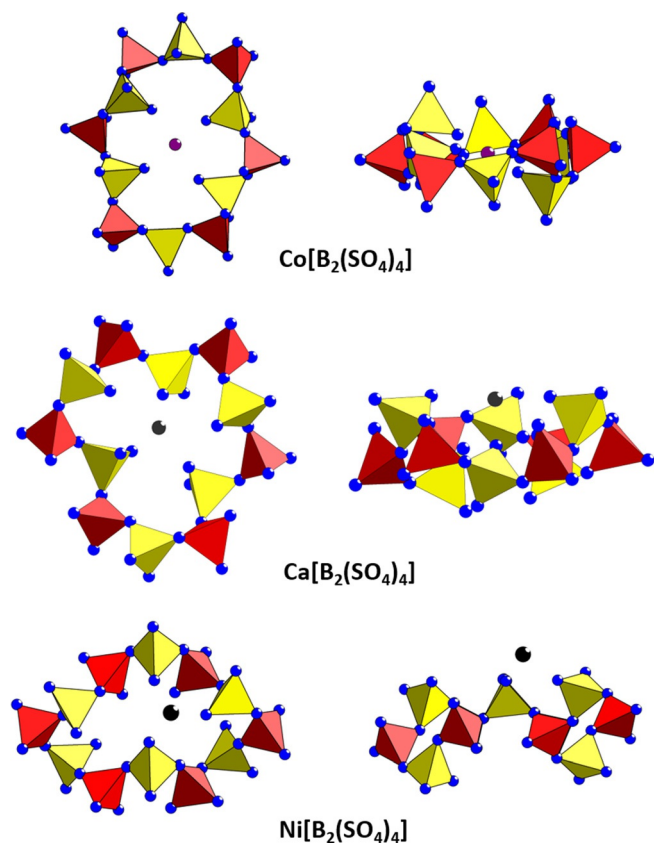


Figure 6. Position of the charge compensating cations Co^{II} (top), Ca^{II} (middle), and Ni^{II} (bottom) in comparison to the center of the *zwölfer* rings in the respective borosulfate Co[B₂(SO₄)₄], Ca[B₂(SO₄)₄], and Ni[B₂(SO₄)₄]. Left: Projection on top of the *zwölfer* rings; Right: Lateral projection of the *zwölfer* rings.

($\mu_{\text{eff}} = 4.27(1) \mu_{\text{B}}$),^[14] Co₂P₄O₁₂ ($\mu_{\text{eff}} = 5.16 \mu_{\text{B}}$)^[15,16] or CoSO₄ ($\mu_{\text{eff}} = 5.65 \mu_{\text{B}}$).^[17] The effective magnetic moment of Ni[B₂(SO₄)₄] in contrast is lower than expected ($\mu_{\text{calc}}(\text{Ni}^{2+}) = 2.83 \mu_{\text{B}}$) and might be explained by diamagnetic impurities, for example, H₂SO₄, adhered to the sample. The low-field measurements conducted in zero-field-cooled/ field-cooled mode (ZFC/FC) mode are depicted in Figures 7 and 8 (middle). Both compounds exhibit an antiferromagnetic anomaly with $T_{\text{N,imp}} = 7.3(1) \text{ K}$ for the Co-compound and $T_{\text{N}} = 3.3(1) \text{ K}$ for the Ni-representative. The increase of the susceptibility of Co[B₂(SO₄)₄] after the anomaly, however, suggests that this anomaly is an antiferromagnetically ordered impurity rather than a bulk phenomenon (and is already suppressed in the 10 kOe measurement). Another possibility that could also be ruled out would be an antiferromagnetic ground state along with a very low critical field (meta-magnetic transition). The 3 K isotherm shows a monotonic increase in the low-field regime without any S-shape, in contrast to the nickel compound.

For Ni[B₂(SO₄)₄] the anomaly is intrinsic. This interpretation is further underlined by the magnetization isotherms recorded at 3 K, shown in Figures 7 and 8 (bottom). While the isotherm in the case of Co[B₂(SO₄)₄] shows almost the ideal trend for a paramagnetic compound at low temperatures (at low fields an anomaly is visible caused by the impurity), the trace of

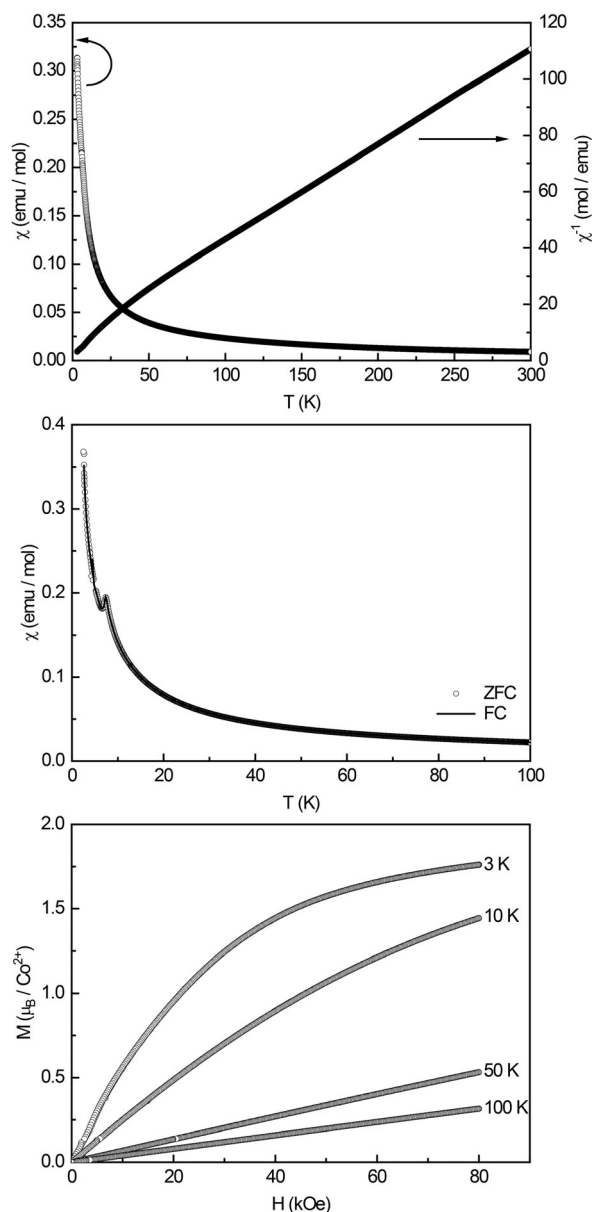


Figure 7. Magnetic data of Co[B₂(SO₄)₄]. (top) magnetic and inverse magnetic susceptibility (χ and χ^{-1} data), measured at an applied external field of 10 kOe; (middle) low-field measurements conducted in zero-field-cooled/ field-cooled mode (ZFC/FC) with an applied field of 100 Oe; (bottom) magnetization isotherms recorded at 3, 10, 50 and 100 K.

Ni[B₂(SO₄)₄] exhibits a pronounced S-shape. This feature is a so-called *meta*-magnetic step, also known as spin-reorientation from an antiparallel to a parallel spin alignment forced by the applied external magnetic field. While the 10 K isotherm for Co[B₂(SO₄)₄] is still slightly curved, all other isotherms for both compounds are linear, in line with the typical paramagnetic behavior. The saturation magnetizations reach $\mu_{\text{sat}} = 1.76(1) \mu_{\text{B}}$ (Co) and $\mu_{\text{sat}} = 1.71(1) \mu_{\text{B}}$ (Ni) at 3 K and 80 kOe, which is below the expected values of $\mu_{\text{sat}} = 3.87(1) \mu_{\text{B}}$ (Co) and $\mu_{\text{sat}} = 2.83(1) \mu_{\text{B}}$ (Ni), caused by the polycrystalline sample and the limited field strength.

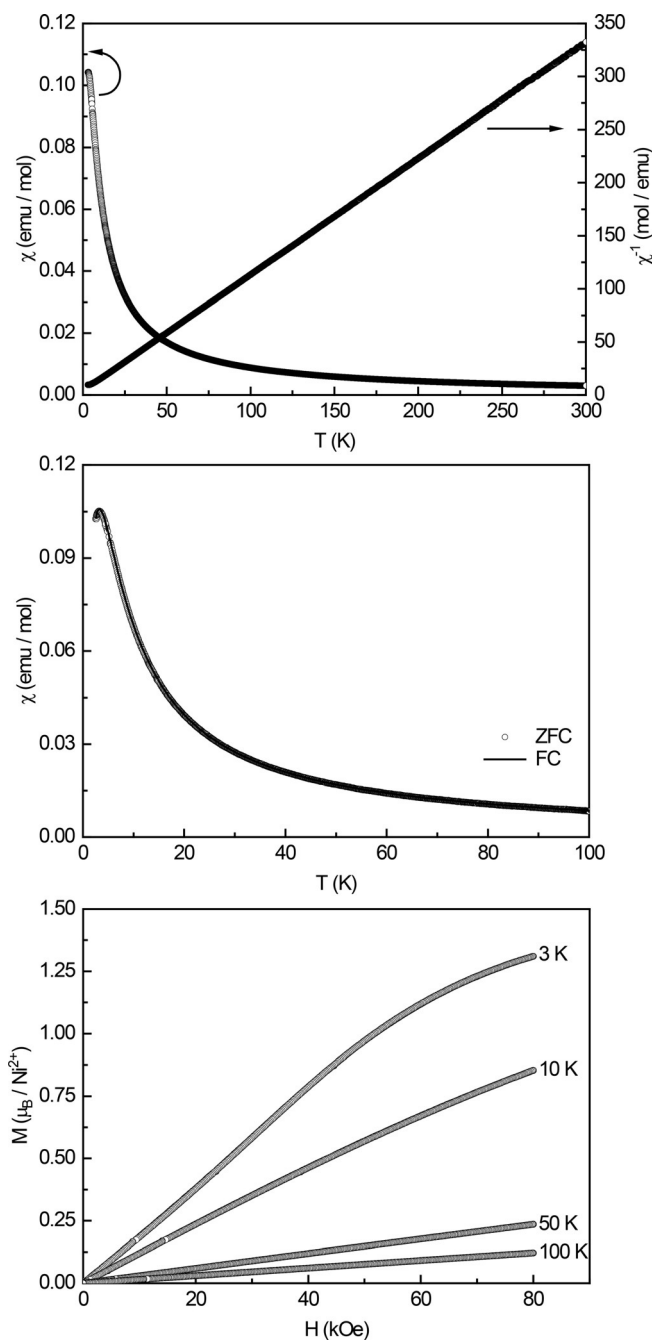


Figure 8. Magnetic data of $\text{Ni}[\text{B}_2(\text{SO}_4)_4]$. (top) magnetic and inverse magnetic susceptibility (χ and χ^{-1} data), measured at an applied external field of 10 kOe; (middle) low-field measurements conducted in zero-field-cooled/field-cooled mode (ZFC/FC) with an applied field of 100 Oe; (bottom) magnetization isotherms recorded at 3, 10, 50 and 100 K.

XPS measurements

Based on the magnetic measurements alone, the oxidation state of Co could not unambiguously be determined as the measured magnetic moment was higher than the theoretical value for Co^{2+} . Hence, XPS measurements were performed using crystals of $\text{Co}[\text{B}_2(\text{SO}_4)_4]$ in order to check film composition and oxidation states of the Co.

Often when using XPS, the oxidation states of a given element in a sample is determined by the absolute binding energy of characteristic core level states; this can be unreliable, as in many cases a wide range of values can be found in literature. For transition metal oxides with open d-shells, the oxidation state can be determined accurately by the presence of satellite peaks in the core level spectra. Upon photoexcitation of an electron out of the strongly bound p-state, a hole is created. As for example discussed by Gupta and Sen,^[18] unpaired d-electrons can interact with this hole, resulting in various final state configurations which differ in energies. This leads to the presence of shake-up peaks in the XPS spectra of transition metals with unpaired electrons, making it possible to distinguish for example, the open shell Co^{II} from a closed shell Co^{III} ; in the latter case, no shake-up peaks are expected.^[19] Figure 9 shows the Co 2p region with its spin-orbit split $2p_{3/2}$ and $2p_{1/2}$ features at binding energies of 782.27 and 798.51 eV, respectively. In addition, both peaks have a strong shake-up feature, shifted to higher binding energy by 4.0 eV with respect to the main peak, which confirms the expected oxidation state of Co^{II} being present.^[19]

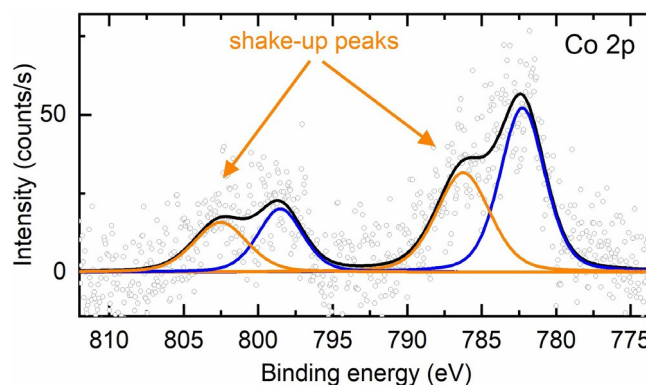


Figure 9. XPS core level spectrum of Co 2p region for $\text{Co}[\text{B}_2(\text{SO}_4)_4]$. After background subtraction, the region was fitted using four Voigt profiles. Blue peaks correspond to the main $2p_{1/2}$ and $2p_{3/2}$ features, while orange ones mark the shake-up features induced by the interaction with the unpaired 3d electron in the Co^{II} oxidation state. The black curve presents the overall fit to the data (open circles).

Quantum chemical investigations of $\text{Ni}[\text{B}_2(\text{SO}_4)_4]$ and $\text{Co}[\text{B}_2(\text{SO}_4)_4]$

To further characterize the new divalent borosulfates, quantum chemical investigations were performed. Fully optimized crystal structures agree very well with the experimental X-ray structural data as evident from comparison of the unit cell parameters listed in Table S9. To assess the electronic structures of the two new solids, high-spin (hs) and low-spin (ls) states were converged. However, for both borosulfates, the high-spin states are energetically more favorable ($\Delta E_{\text{hs-ls}} > 300 \text{ kJ mol}^{-1}$), which is in line with the magnetochemical measurements that found paramagnetic behavior.

A Hirshfeld population analysis corroborated divalent cations, positively charged sulfur and boron atoms as well as neg-

atively charged oxygen atoms as listed in Table 3. These findings show little dependence on the density functional as all three essentially yield the same results. They also agree with earlier investigations of various divalent borosulfates^[8f] including those of phyllosilicate type.^[8b]

Calculated IR and Raman spectra (see Supporting Information Figures S6–S7 and Tables S10–S11) also show the typical borosulfate signatures: S–O and B–O stretching modes are found above 870 cm⁻¹, bending modes of $\delta(\text{OSO})$, $\delta(\text{OBO})$, and $\delta(\text{SOB})$ dominate in the regime between 900 and 350 cm⁻¹, and Ni–O and Co–O stretching and bending modes prevail below 400 cm⁻¹. These results are in line with those found for other phyllosilicate type borosulfates^[8b] and once more indicate their close chemical relationship.

Despite these similarities distinct differences in the position of the divalent cation with respect to the anionic borosulfate layers are found. Ni^{II} prefers a position between the layers, whereas Co^{II} is located in the layer. In fact, besides Ni^{II} (and the isotopic Mg[B₂(SO₄)₄]), Ca is the only other divalent cation that prefers a position between the borosulfate layer, while in all other known phyllosilicate type borosulfates the cation is located within the anionic layer.

To assess the origin of this structural preference, in an in silico experiment Ni^{II} and Co^{II} were replaced in their respective crystal structures by Ca^{II} and the structures were optimized. Two distinct structures were converged, but an analysis of the electronic energy revealed that Ca^{II} prefers neither of these positions and both in silico structures have a higher relative

energy ($\approx +80$ kJ mol⁻¹) than observed for the Ca^{II} in its experimentally found (and quantum chemically optimized) crystal structure. Thus, Ca^{II} has no tendency to reside on the Ni^{II} position and does not like to relax into the layer either (compare Figure 3). This can be rationalized by the size (ionic radius of 1.26 Å) and the number of coordination partners (here eight) that is very different from all other borosulfates.

Next, Co^{II} was replaced by Ni^{II} and the such obtained Ni^{II} borosulfate with the charge compensating cations in the layer was optimized. Again, an in silico structure, where Ni^{II} is situated in the borosulfate layer could be converged but this structure is less stable than the one with Ni^{II} between the layers (see Table 4). The results for both density functionals are very similar. Thus, the discussion is restricted to the results obtained with HSESOL only, while the reader is referred to Table S12 for the PBESOL results. Surprisingly, replacement of Ni^{II} by Co^{II}, leading to a structure where Co^{II} is situated between the layer, showed that this arrangement is energetically preferred. The influence of the electron configuration of Co^{II} was also tested but both, the high-spin and the low-spin state prefer the Ni^{II} position, that is, between the borosulfate layers. Hence, the spin state does not impact nor determine the position of the cation. It is noteworthy, that the low-spin state is again significantly higher in energy than the high-spin state (+300 kJ mol⁻¹ for HSESOL Co^{II} on Ni^{II} position).

To check whether the energetic preference of the cation to occupy a position outside the anionic borosulfate layer is systematic or just a peculiarity of Co^{II}, the two other phyllosilicate type borosulfates with charge compensating cations located within the layer were investigated too. These are Zn[B₂(SO₄)₄]^[11] and Mn[B₂(SO₄)₄]^[11]. Ni^{II} was replaced by Zn^{II}, and Mn^{II}, respectively, and the two in silico structures were optimized. In addition, as Mg[B₂(SO₄)₄] is isotopic to Ni[B₂(SO₄)₄] with the charge compensation cations located between the layers, the Co^{II} atoms in Co[B₂(SO₄)₄] were also replaced by Mg^{II} yielding another in silico modification. Results of these optimizations are summarized in Table 4. Indeed, neither Zn^{II} nor Mn^{II} relaxed back into the borosulfate layer but for both stable conformations with the cation between the layers were found. Unexpectedly, also for Zn^{II} a position between the borosulfate layers is energetically favored over the experimentally found position within the layers, while for Mn^{II} both positions are very similar in energy. Similarly, Mg^{II} prefers its position be-

Table 3. Hirshfeld population analysis for Ni[B₂(SO₄)₄] and Co[B₂(SO₄)₄] obtained with different density functionals. Results for the high-spin states (Ni: *d*⁶ and Co: *d*⁷) are depicted (for details see Quantum chemical methodology).

	M	S	O	B
Ni				
PBESOL	+1.85	+2.07–+2.20	-0.94–-0.64	+1.32
HSESOL	+1.96	+2.34–+2.48	-1.03–-0.72	+1.51
B3LYP	+1.95	+2.33–+2.46	-1.02–-0.72	+1.55
Co				
PBESOL	+1.92	+2.07–+2.21	-0.99–-0.65	+1.28
HSESOL	+2.03	+2.34–+2.48	-1.02–-0.74	+1.48–+1.49
B3LYP	+1.96	+2.32–+2.45	-1.00–-0.74	+1.51

Table 4. Relative stabilities of various phyllosilicate type borosulfates. In the left columns results for structures with the charge compensating cation between the borosulfate layers are shown, whereas in the right columns structures with the cation situated within the borosulfate layer are listed. "Opt. exp. struc." denotes the relative energy of the optimized crystal structure, "Opt. in silico" denotes the energy of an in silico structure. Ionic radii are given in Å. Results were obtained with the HSESOL density functional. Energies are given in kJ mol⁻¹.

	Cation between layer		Cation within layer		
	Ni[B ₂ (SO ₄) ₄]	Mg[B ₂ (SO ₄) ₄]	Co[B ₂ (SO ₄) ₄]	Zn[B ₂ (SO ₄) ₄]	Mn[B ₂ (SO ₄) ₄]
Opt exp. struct.	0.0	0.0	0.0	0.0	0.0
Opt in silico ^[a]	31.4 ^[b]	27.7 ^[b]	-26.6 ^[c]	-22.2 ^[c]	4.4 ^[c]
Ionic radius ^{[d][20]}	0.83	0.86	0.89(hs)/0.79(ls) ^[e]	0.88	0.97(hs) ^[e]

[a] optimized in silico structure. [b] Co replaced by M, M=(Ni, Mg), optimization on experimental Co[B₂(SO₄)₄] structure with M located within the layer. [c] Ni replaced by M, M=(Co, Zn, Mn), optimization on experimental Ni[B₂(SO₄)₄] structure with M located between the layers. [d] for the oxidation state +2 and an octahedral coordination. [e] hs: high-spin, ls: low-spin.

tween the layers and a structure with Mg^{II} within the borosulfate layer is not favored (see Table 4).

To rationalize these findings, we would like to emphasize that Mn^{II} has with $r=0.97$ Å the largest ionic radius of all investigated octahedrally coordinated divalent cations, while all other cations have ionic radii of 0.89 Å (in their high-spin states) or smaller. This may point to the preference of larger ions to adopt a position within the borosulfate layer. Based on our investigations, we furthermore propose the existence of new Zn^{II}, Mn^{II}, and Co^{II} phyllosilicate-type borosulfate phases, where the charge compensating cations occupies a position between the anionic layers.

Conclusions

We reported two new transition-metal containing borosulfates of the phyllosilicate type, Ni[B₂(SO₄)₄] and Co[B₂(SO₄)₄], where vertex-linked (BO₄)- and (SO₄)-tetrahedra form a 2D anion, charge balanced by the divalent cations. These add to the family of phyllosilicate analogue borosulfates, which are still poorly investigated. The anionic substructures are very similar, the structural difference of Ni[B₂(SO₄)₄] and Co[B₂(SO₄)₄] are mainly due to the position of the charge compensating cations.

Magnetochemical studies confirmed the open-shell high-spin state, where Ni^{II} has two and Co^{II} three unpaired electrons, as found in most octahedral coordination environments. The oxidation state of Co was furthermore confirmed by XPS analysis.

Quantum chemical studies are fully consistent with the experimental findings. They further corroborate the typical borosulfate characteristics, that is, a charge distribution, where S and B are positively charged, while O is negatively charged. The calculated vibrational signatures agree with those of other borosulfates. In accordance with magnetic measurements, the energetically most favored state of Ni and Co is high-spin.

By exchange of the metal cations in *in silico* experiments, we unveiled systematic trends in the series of borosulfates concerning the position of the charge balancing ion: in contrast to previous experimental findings, cations with a small ionic radius show a tendency to be situated between the borosulfate layer, thus not only Ni^{II} and Mg^{II} but also Co^{II} and Zn^{II} prefer this position. Our results suggest that with increasing ionic radii, the cation position within a layer becomes more favorable for divalent cations. These findings led us to propose new phyllosilicate type borosulfate structures giving hints for new materials and an ever expanding class of silicate analogues.

Experimental Section

Synthesis of Ni[B₂(SO₄)₄] and Co[B₂(SO₄)₄]: H₃BO₃ (99.8%, 300 mg, Carl Roth, Karlsruhe, Germany), 1 mL oleum (65% SO₃, Sigma-Aldrich, Darmstadt, Germany) and NiO (99.9%, 50 mg, Strem Chemicals, Kehl, Germany) for Ni[B₂(SO₄)₄] or Co₃O₄ (99.5%, 50 mg, Fluka, München, Germany) for Co[B₂(SO₄)₄] were loaded into a thick-walled borosilicate glass ampoule (l=300 mm, Ø=16 mm, thick-

ness of the tube wall=1.8 mm). The ampoules were torch sealed, placed into a tube furnace and heated up to 523 K. The temperature was maintained for 24 hours and finally reduced to 298 K with a cooling rate of 0.1 K min⁻¹. A large number of yellow crystals (Figure S1) for Ni[B₂(SO₄)₄] and violet crystals (Figure S2) for Co[B₂(SO₄)₄] were obtained. The crystals are very moisture sensitive and decompose immediately after exposure to air. Thus, the products were handled strictly under inert conditions.

Caution: Oleum is a strong oxidizer and needs careful handling. During and even after the reaction the ampoule might be under remarkable pressure. It is mandatory to cool down the ampoule by liquid nitrogen prior to opening.

X-ray crystallography: The mother liquor was separated from the crystals via decantation, the acid containing side of the ampoule was cooled with liquid nitrogen and several crystals were transferred into inert oil directly after opening. The remaining bulk material was transferred to the glovebox for further characterization. Under a polarization microscope, a suitable crystal was selected and mounted onto a glass needle (Ø=0.1 mm) and immediately placed into a stream of cold N₂ inside the diffractometer (Bruker D8 Quest κ, Bruker, Karlsruhe, Germany), respectively. After unit cell determination, the intensity data was collected. Structure solution and refinements were conducted with the SHELX program package.^[21]

Further details of the crystal structure investigations may be obtained from the joint CCDC/FIZ Karlsruhe online deposition service by quoting the deposition numbers CSD-1894893, and 1907638.

Ni[B₂(SO₄)₄]: The crystal structure of Ni[B₂(SO₄)₄] was solved in the monoclinic crystal system in the space group C2/c. The heavy atom positions were determined by SHELXS-2008^[21] using Direct Methods. Further atoms could be successfully located by difference Fourier techniques during refinement with SHELXL-2013.^[22] A multi-scan absorption correction was applied to the data using the program SADABS-2014/5.^[23] Finally, the structure and model were refined to $R_1=0.0384$ and $wR_2=0.0591$ for all data. Selected bond lengths and angles are presented in the Tables S3 and S4.

Co[B₂(SO₄)₄]: The crystal structure of Co[B₂(SO₄)₄] was also solved in the monoclinic crystal system in the space group P2₁/n. The heavy atom positions were determined by SHELXT-2014/4^[24] using Direct Methods. Further atoms could be successfully located by difference Fourier techniques during refinement with SHELXL-2014/7.^[22] A multi-scan absorption correction was applied to the data using the program SADABS-2014/5.^[23] Finally, the structure and model refined to $R_1=0.0181$ and $wR_2=0.0462$ for all data. Selected bond lengths and angles are presented in the Tables S7 and S8.

Prior to all following measurements, the samples were washed with dry CCl₄ and dried under reduced pressure to remove remaining amounts of adhesive oil.

X-ray powder diffraction: The measurements were carried out with a Stoe Stadi P powder diffractometer in transmission geometry. The flat sample was irradiated with Ge(111)-monochromatized Mo_{Kα1}-radiation ($\lambda=0.7093$ Å), which was detected by means of a Dectris Mythen 1 K detector. Rietveld refinement was accomplished using TOPAS 4.2.^[25] The diffraction patterns are shown in Figure S5.

Magnetochemical investigations: The crystalline samples of Co[B₂(SO₄)₄] and Ni[B₂(SO₄)₄] were packed into polyethylene (PE) capsules in an argon filled drybox and attached to the sample holder rod of a Vibrating Sample Magnetometer (VSM) for measuring the magnetization $M(T,H)$ in a Quantum Design Physical Property Measurement System (PPMS). The samples were investigated in the temperature range of 2.5–300 K with applied external magnetic fields up to 80 kOe.

X-ray photoelectron spectroscopy: For this investigation, the crystallites of $\text{Co}[\text{B}_2(\text{SO}_4)_4]$ were pressed onto a conductive copper tape and loaded into the ultra-high vacuum system without air exposure. The measurements were carried out using a non-monochromatic $\text{Al}_{K\alpha}$ X-ray source (VG) at $h\nu = 1486.6$ eV. The kinetic energy of the electrons was recorded using a hemispherical analyzer (Phoibos 100, Specs) at 15 eV pass energy under normal emission. Peak fits were performed using the XPSPEAK41 software, employing Voigt line shapes and a linear background that is subtracted in the data shown in Figure 9.

Quantum chemical methodology: The experimentally obtained X-ray crystal structures of $\text{Ni}[\text{B}_2(\text{SO}_4)_4]$ and $\text{Co}[\text{B}_2(\text{SO}_4)_4]$ were used as starting conformations for the quantum chemical investigations. Both structures were fully optimized using Density Functional Theory with periodic boundary conditions as implemented in CRYSTAL17.^[26] Three different density functionals, the pure PBESOL,^[27] the range-separated hybrid HSE03,^[28a] and the hybrid B3LYP^[28b] density functionals were used together with all-electron basis sets for all atoms: Ni,^[29] Co,^[30] Zn,^[31] Mn,^[29] Mg,^[32] S,^[33] O,^[29] B,^[34] whereas for Ca effective core potentials were used in addition.^[35] For the borosulfates, spin-unrestricted open-shell calculations were performed for a high-spin state as well as for a low-spin state (in case of Ni this is a closed-shell configuration) to evaluate which spin state is energetically favored. Analyses of the electronic structures were complemented by an iterative Hirshfeld population analysis as implemented in CRYSTAL17.^[26] Here, the partial charge at each atom results from the difference of the total electronic density and a promolecular atomic density.

Acknowledgements

We thank Assoz.-Prof. Dr. Gunter Heymann for the single-crystal X-ray investigation. The computational results presented have been achieved using the HPC infrastructure of the University of Innsbruck and the MACH2 Interuniversity Shared Memory Supercomputer. J.B. is thankful to the Fonds der Chemischen Industrie (FCI) for financial support. M.P. acknowledges the Austrian Science Fund FWF (M-2005) for financial support. L.C.P. is grateful for the Ph.D. scholarship from the Leopold-Franzens-University Innsbruck. Open access funding enabled and organized by Projekt DEAL.

Conflict of interest

The authors declare no conflict of interest.

Keywords: cobalt • crystal structure • magnetic properties • nickel • quantum chemistry

- [1] F. Liebau, *Structural Chemistry of Silicates*, Springer, Heidelberg, 1985.
- [2] L. P. Soloveva, V. V. Bakakin, *Zh. Strukt. Khim.* **1966**, *7*, 469–472.
- [3] a) L. Pauling, *Proc. Natl. Acad. Sci. USA* **1930**, *16*, 453–459; b) J. Felsche, S. Luger, Ch. Baerlocher, *Zeolites* **1986**, *6*, 367–372; c) J. B. Jones, *Acta Crystallogr. Sect. B* **1968**, *24*, 355–358.
- [4] a) M. Mofarrah, F. Gholipour, *Microporous Mesoporous Mater.* **2014**, *200*, 1–10; b) J. Vermesse, D. Vidal, P. Malbrunot, *Langmuir* **1996**, *12*, 4190–4196; c) P. Li, H. Tezel, *Microporous Mesoporous Mater.* **2007**, *98*, 94–101; d) R. V. Siriwardane, M.-S. Shen, E. P. Fisher, *Energy Fuels* **2003**, *17*, 571–576; e) V. J. Inglezakis, *J. Colloid Interface Sci.* **2005**, *281*, 68–79; f) S.-T. Yang, J. Kim, W. S. Ahn, *Microporous Mesoporous Mater.* **2010**, *135*, 90–94.

- [5] a) S. Oliver, A. Kupermann, G. A. Ozin, *Angew. Chem. Int. Ed.* **1998**, *37*, 46–62; *Angew. Chem.* **1998**, *110*, 48–64; b) S. T. Wilson, B. M. Lok, C. A. Messina, T. R. Cannan, E. M. Flanigen, *J. Am. Chem. Soc.* **1982**, *104*, 1146–1147; c) S. Oliver, A. Kuperman, A. Lough, G. A. Ozin, *Chem. Mater.* **1996**, *8*, 2391–2398; d) S. Oliver, A. Kuperman, A. Lough, G. A. Ozin, *Inorg. Chem.* **1996**, *35*, 6373–6380; e) A. Kuperman, S. Nadimi, S. Oliver, G. A. Ozin, J. M. Garces, M. M. Olken, *Nature* **1993**, *365*, 239–242; f) R. Kniep, M. Steffen, *Angew. Chem. Int. Ed. Engl.* **1978**, *17*, 272–273; *Angew. Chem.* **1978**, *90*, 286–286.
- [6] a) R. Kniep, H. Engelhardt, C. Hauf, *Chem. Mater.* **1998**, *10*, 2930–2934; b) R. P. Bontchev, S. C. Sevov, *Inorg. Chem.* **1996**, *35*, 6910–6911; c) S. C. Sevov, *Angew. Chem. Int. Ed. Engl.* **1996**, *35*, 2630–2632; *Angew. Chem.* **1996**, *108*, 2814–2816; d) I. Boy, F. Stowasser, G. Schäfer, R. Kniep, *Chem. Eur. J.* **2001**, *7*, 834–839; e) E. A. Ruchkina, E. L. Belokoneva, *Russ. J. Inorg. Chem.* **2003**, *48*, 1812–1821; f) R. Kniep, H. Engelhardt, *Z. Anorg. Allg. Chem.* **1998**, *624*, 1291–1297; g) O. A. Gurbanova, E. L. Belokoneva, *Crystallogr. Rep.* **2007**, *52*, 624–633; h) R. Kniep, G. Schäfer, H. Engelhardt, I. Boy, *Angew. Chem. Int. Ed.* **1999**, *38*, 3641–3644; *Angew. Chem.* **1999**, *111*, 3857–3861.
- [7] H. A. Höpfe, K. Kazmierczak, M. Daub, K. Förg, F. Fuchs, H. Hillebrecht, *Angew. Chem. Int. Ed.* **2012**, *51*, 6255–6257; *Angew. Chem.* **2012**, *124*, 6359–6362.
- [8] a) M. Daub, K. Kazmierczak, P. Gross, H. Höpfe, H. Hillebrecht, *Inorg. Chem.* **2013**, *52*, 6011–6020; b) J. Bruns, M. Podewitz, M. Schauerl, B. Joachim, K. Liedl, H. Huppertz, *Chem. Eur. J.* **2017**, *23*, 16773–16781; c) M. Daub, H. A. Höpfe, H. Hillebrecht, *Z. Anorg. Allg. Chem.* **2014**, *640*, 2914–2921; d) P. Gross, A. Kirchhain, H. A. Höpfe, *Angew. Chem. Int. Ed.* **2016**, *55*, 4353–4355; *Angew. Chem.* **2016**, *128*, 4426–4428; e) L. Dong, S. Pan, Y. Wang, H. Yu, Y. Lin, S. Han, *Mater. Res. Bull.* **2015**, *63*, 93–98; f) J. Bruns, M. Podewitz, O. Janka, R. Pöttgen, K. Liedl, H. Huppertz, *Angew. Chem. Int. Ed.* **2018**, *57*, 9548–9552; *Angew. Chem.* **2018**, *130*, 9693–9697; g) P. Netzsch, M. Hämmer, P. Gross, H. Bariss, T. Block, L. Helletta, R. Pöttgen, J. Bruns, H. Huppertz, H. A. Höpfe, *Dalton Trans.* **2019**, *48*, 4387–4397; h) M. Daub, K. Kazmierczak, H. A. Höpfe, H. Hillebrecht, *Chem. Eur. J.* **2013**, *19*, 16954–16962; i) J. Bruns, M. Podewitz, M. Schauerl, K. Liedl, O. Janka, R. Pöttgen, H. Huppertz, *Eur. J. Inorg. Chem.* **2017**, 3981–3989; j) S. Schönegger, J. Bruns, B. Gartner, K. Wurst, K. Liedl, H. Huppertz, *Z. Anorg. Allg. Chem.* **2018**, *644*, 1702–1706.
- [9] a) C. Logemann, M. S. Wickleder, *Angew. Chem. Int. Ed.* **2013**, *52*, 14229–14232; *Angew. Chem.* **2013**, *125*, 14479–14482; b) M. Daub, H. Hillebrecht, *Eur. J. Inorg. Chem.* **2015**, 4176–4181; c) P. Netzsch, P. Gross, H. Takahashi, S. Lotfi, J. Brgoch, H. A. Höpfe, *Eur. J. Inorg. Chem.* **2019**, 3975–3981; d) P. Netzsch, P. Gross, H. Takahashi, H. A. Höpfe, *Inorg. Chem.* **2018**, *57*, 8530–8539.
- [10] J. Bruns, H. A. Höpfe, M. Daub, H. Hillebrecht, H. Huppertz, *Chem. Eur. J.* **2020**, *26*, 7966–7980.
- [11] L. C. Pasqualini, H. Huppertz, J. Bruns, *Inorganics* **2019**, *7*, 145–154.
- [12] B. Ewald, Y.-X. Huang, R. Kniep, *Z. Anorg. Allg. Chem.* **2007**, *633*, 1517–1540.
- [13] G. A. Bain, J. F. Berry, *J. Chem. Educ.* **2008**, *85*, 532–536.
- [14] S. D. Kloß, O. Janka, T. Block, R. Pöttgen, R. Glaum, W. Schnick, *Angew. Chem. Int. Ed.* **2019**, *58*, 4685–4689; *Angew. Chem.* **2019**, *131*, 4733–4737.
- [15] K. Rohwer, A. Wiedenmann, W. GunBer, *Physica B* **1986**, *136*, 341–345.
- [16] W. GunBer, D. Fruehauf, K. Rohwer, A. Zimmermann, A. Wiedenmann, *J. Solid State Chem.* **1989**, *82*, 43–51.
- [17] B. C. Frazer, P. J. Brown, *Phys. Rev.* **1962**, *125*, 1283–1291.
- [18] R. P. Gupta, S. K. Sen, *Phys. Rev. B* **1974**, *10*, 71–77.
- [19] M. C. Biesinger, B. P. Payne, A. P. Grosvenor, L. W. M. Lau, A. R. Gerson, R. St. C. Smart, *Appl. Surf. Sci.* **2011**, *257*, 2717–2730.
- [20] A. F. Holleman, N. Wiberg, *Lehrbuch der Anorganischen Chemie*, de Gruyter, Berlin, 2007.
- [21] G. M. Sheldrick, *Acta Crystallogr. Sect. A* **2008**, *64*, 112–122.
- [22] G. M. Sheldrick, *Acta Crystallogr. Sect. C* **2015**, *71*, 3–8.
- [23] G. M. Sheldrick, SADABS 2014/5, University of Göttingen: Göttingen, Germany, 1996.
- [24] G. M. Sheldrick, *Acta Crystallogr. Sect. A* **2015**, *71*, 3–8.
- [25] TOPAS4.2, Bruker, Karlsruhe, Germany, 2009.
- [26] a) R. Dovesi, V. R. Saunders, C. Roetti, R. Orlando, C. M. Zicovich-Wilson, F. Pascale, B. Civalleri, K. Doll, N. M. Harrison, I. J. Bush, P. D'Arco, M. Llunell, M. Causà, Y. Noël, L. Maschio, A. Erba, M. Rerati, S. Casassa, CRY-

- TAL17 User's Manual*, University of Torino, Torino, **2017**; b) R. Dovesi, A. Erba, R. Orlando, C. M. Zicovich-Wilson, B. Civalleri, L. Maschio, M. Rerat, S. Casassa, J. Baima, S. Salustro, B. Kirtman, *Wires Comput. Mol. Sci.* **2018**, *8*, e1360.
- [27] J. P. Perdew, A. Ruzsinszky, G. I. Csonka, O. A. Vydrov, G. E. Scuseria, L. A. Constantin, X. L. Zhou, K. Burke, *Phys. Rev. Lett.* **2008**, *100*, 136406.
- [28] a) L. Schimka, J. Harl, G. Kresse, *J. Chem. Phys.* **2011**, *134*, 024116; b) A. D. Becke, *J. Chem. Phys.* **1993**, *98*, 5648–5652.
- [29] M. D. Towler, N. L. Allan, N. M. Harrison, V. R. Saunders, W. C. Mackrodt, E. Apra, *Phys. Rev. B* **1994**, *50*, 5041–5054.
- [30] R. Dovesi, F. F. Fava, C. Roetti, V. R. Saunders, *Faraday Discuss.* **1997**, *106*, 173–187.
- [31] J. E. Jaffe, A. C. Hess, *Phys. Rev. B* **1993**, *48*, 7903–7909.
- [32] M. F. Peintinger, D. V. Oliveira, T. Bredow, *J. Comput. Chem.* **2013**, *34*, 451–459.
- [33] A. Lichanot, E. Apra, R. Dovesi, *Phys. Status Solidi B* **1993**, *177*, 157–163.
- [34] R. Orlando, R. Dovesi, C. Roetti, V. R. Saunders, *J. Phys. Condens. Matter* **1990**, *2*, 7769–7789.
- [35] M. P. Habas, R. Dovesi, A. Lichanot, *J. Phys. Condens. Matter* **1998**, *10*, 6897–6909.

Manuscript received: May 5, 2020

Accepted manuscript online: June 17, 2020

Version of record online: October 22, 2020